Journal of Nuclear Materials 385 (2009) 572–581

Contents lists available at ScienceDirect

Journal of Nuclear Materials

journal homepage: www.elsevier.com/locate/jnucmat

Thermal effects in 10 keV Si PKA cascades in 3C–SiC

David E. Farrell [a,1], Noam Bernstein [c], Wing Kam Liu [b,*]

[a] Department of Materials Science and Engineering, Northwestern University, 2220 Campus Dr., Evanston, IL 60208, USA
[b] Department of Mechanical Engineering, Northwestern University, 2145 Sheridan Rd., Suite, B224, Evanston, IL 60208, USA
[c] Center for Computational Materials Science, Code 6392 Naval Research Laboratory, 4555 Overlook Ave. SW, Washington, DC 20375, USA

ARTICLE INFO

Article history:
Received 28 October 2008
Accepted 8 January 2009

ABSTRACT

We present a molecular dynamics study of the influence of temperature on defect generation and evolution in irradiated cubic silicon carbide. We simulated 10 keV displacement cascades, with an emphasis on the quantification of the spatial distribution of defects, at six different temperatures from 0 K to 2000 K under identical primary knock-on atom conditions. By post-processing the simulation results we analyzed the temporal evolution of vacancies, interstitials, and antisite defects, the spatial distribution of vacancies, and the distribution of vacancy cluster sizes. The majority of vacancies were found to be isolated at all temperatures. We found evidence of temperature dependence in C and Si replacements and C_{Si} antisite formation, as well as reduced damage generation behavior due to enhanced defect relaxation at 2000 K.

1. Introduction

Point defects can be generated in particle irradiated crystalline solids as a result of collisions initiated by the irradiating particle. This mode of damage is often referred to as *displacement damage*, and it can lead to localized microstructural modification and thus mechanical property changes [1]. Irradiation effects on solids have received a great deal of attention as far back as the 1960s [2,3]. This attention was predominantly related to metals, though more recently interest has grown in crystalline non-metals [4] such as SiC-based composite materials and coatings [5–8].

There is relatively little information available on displacement damage effects in SiC and SiC-based composites compared to metals and Si [5]. In monolithic SiC and SiC composites, at temperatures lower than approximately 1300 K, isotropic expansion (swelling) of the material is a relatively well known phenomenon [9–11,7]. Other phenomena include void formation and subsequent swelling at temperatures up to approximately 1800 K [12,7]. Despite a wide range of phenomenological studies performed on SiC, the microstructural events responsible for these observed macroscopic phenomena are not well understood [13]. Specifically, it has been noted that further investigation is required with respect to radiation effects on defect production and evolution in SiC [14,5,15]. Thus, we believe it is of significant technological interest to elucidate and quantify point defect generation and evolution as a result of particle radiation in this material. In particular, we chose to study 3C–SiC, one of the polytypes being considered for advanced energy applications because of properties such as high strength, high thermal conductivity and low chemical reactivity. In 3C–SiC, the Si–C bi-layers are stacked like those in a face-centered cubic crystal (i.e., ABCABC stacking along $\langle 1\,1\,1 \rangle$) as in Fig. 1.

Empirical potential molecular dynamics (MD) studies into the defect energetics of 3C–SiC were performed by Huang and Ghoniem [16]. Investigations into the threshold displacement energy (TDE) for 3C–SiC were performed by Wong et al. [17] as well as by Devanathan et al. [18] and Hensel et al. [19]. These later works made use of hybrid empirical potentials based on the Tersoff potential [20]. Hensel et al. used the SiC parameter set from [20] and smoothly connected the Tersoff potential to the Ziegler, Biersack and Littmark (ZBL) 'universal' short-range potential [21] to more accurately represent the behavior at small interatomic separations. Devanathan et al. made use of a cubic spline fitted to *ab initio* quantum mechanical results and connected this via a smoothing function to the Tersoff potential with parameters given in Table 1 and [20]. In the Devanathan et al. study, the range for the C TDE was reported to be 28–71 eV and for Si, 36–113 eV (with an estimated ±1 eV error). The extremes of the TDE measurements were reported to be between the [1 1 1] (Si maximum, C minimum), $[\bar{1}\,\bar{1}\,\bar{1}]$ (C maximum) and [0 0 1] (Si minimum) directions, reflecting the lack of reflection symmetry along those directions.

Devanathan et al. applied their hybrid Tersoff potential to 10 keV cascade simulations in 3C–SiC at 300 K [22]. Their simulation cell consisted of $20 \times 20 \times 60$ 3C–SiC unit cells (roughly 192 000 atoms, .4359 nm lattice parameter), with {0 0 1} boundaries. Their simulations kept the number of atoms and system volume constant, while controlling the temperature of the system

* Corresponding author. Fax: +1 847 491 3915.
E-mail addresses: d-farrell2@northwestern.edu (D.E. Farrell), w-liu@northwestern.edu (W.K. Liu).
[1] Principal corresponding author.

0022-3115/$ - see front matter © 2009 Elsevier B.V. All rights reserved.
doi:10.1016/j.jnucmat.2009.01.036

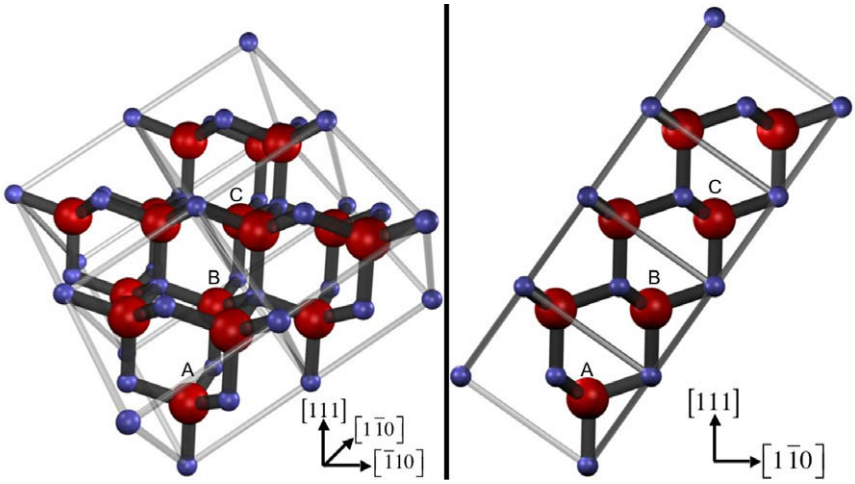

Fig. 1. Schematic of the stacking order 3C–SiC (cubic stacking). 3C–SiC is one of the extremes of the SiC polytypes, and is the only cubic polytype. Miller indices are given to show the crystal orientation. The large and small spheres in each bi-layer denote a silicon and carbon atom, respectively.

through a 4-atom layer thermostat region where the atoms had their velocities rescaled to maintain a temperature of 300 K. They allowed the system to thermally equilibrate for 2 ps prior to exciting the primary knock-on atom (PKA). The 10 keV PKA kinetic energy was imparted to the PKA (a chosen Si atom at the top, center of the simulation cell) in the form of an initial velocity of 262 nm/ps along $[4\,11\,9\bar{5}]$, reportedly to minimize channeling of the PKA. The cascade was allowed to evolve for 10 ps after the PKA excitation, though no explicit timestep information was given. Devanathan et al. reported that the number of interstitials and vacancies slowly increased after the PKA was excited and reached a peak at roughly.1–.3 ps. After this phase, the number of defects decreased to roughly 1/2 of the peak number by roughly .8 ps. Prior to approximately .1 ps, the number of C and Si defects was roughly the same, though as time carried on the number of C defects held steady at roughly three times the number of Si defects. This behavior was attributed to the differences in TDE between C and Si. They also reported that roughly 7% of the displacements led to antisite defects and concluded that this may be an important energy storage mechanism, and may lead to irradiation induced amorphization.

Perlado et al. [23] carried out studies in SiC very similar to those in [22], with a PKA kinetic energy range of .5–8 keV using both C and Si PKAs, at 300 K and 1300 K. Their study also included a study of accumulated damage during multiple irradiation events at 1300 K. They varied their system size from $25 \times 25 \times 25$ (150 000 atoms) to $40 \times 40 \times 60$ (768 000 atoms) 3C–SiC unit cells, depending on the magnitude of the PKA energy, with a 2–4 atom layer thermostat region as in [22]. They reported a final ratio of C to Si vacancies closer to 5:1 than the nearly 3:1 of [22]. They also went on to study the size of the clusters formed by the vacancies. To do this, they identified the number of vacancies within the third-nearest-neighbor distance (.436 nm) of another vacancy. They reported that large clusters of more than a few vacancies rarely occurred in their calculations and that the bulk of the vacancies were isolated from one another. They did not report any temperature dependence in cascade formation or defect production, though they did note that defect mobility was low enough at both 300 K and 1300 K that little re-organization of the defect structure was seen over periods of up to 1 ns.

This paper seeks to build on the work of [22] and [23] in three ways. The first is that we studied the influence of thermal vibrations on cascade formation and evolution, particularly on the spatial distribution of vacancies, through a range of temperatures from 0 K to 2000 K. The second is that our simulations were performed in simulation cells larger than those used in [22] and [23]. The final difference is that the lattice parameter we used in this study was obtained based on the proposed operating temperature and pressure of the ARIES-AT first wall structure [24]. The next section will discuss our simulation and post-processing methodology. This will lead into the discussion of the results for the six temperatures studied and finally, our conclusions.

Table 1
Parameter set for Si and C, as provided by Devanathan et al. [18]. Length parameters S and R were reported to not be optimized and have not been optimized here. Mass taken from [25].

Parameter	Devanathan et al.	
	C	Si
A (eV)	1544.8	1830.8
B (eV)	389.63	471.18
λ (nm^{-1})	34.653	24.799
μ (nm^{-1})	23.064	17.322
β	4.1612×10^{-6}	1.1000×10^{-6}
n	0.99054	.78734
c	19981	100390
d	7.034	16.217
h	−.33953	−.59825
R (nm)	.18	.27
S (nm)	.21	.30
χ_{C-Si}	1.0086	
Mass, m_a (u)	12.0107	28.0855

2. Simulation methodology

To represent a perfect SiC crystal, we used a cube with 50 3C–SiC unit cells per side (1 000 000 atoms total) and {0 0 1} boundaries. We approximated this cube being a small part of a infinite body by enforcing periodic boundary conditions on all sides. To simulate the bulk of the infinite body being at a known temperature, we applied a 4-cell thick velocity-scaled thermostat 'skin' to all sides of the cube except the 'top' (topmost (0 0 1) atom planes). We did not apply the thermostat to the top layer to avoid any artificial reductions in the energy of the PKA and its neighbors at the beginning of the simulation. To obtain the lattice parameter used, we relaxed the system volume while keeping the number of atoms, pressure and temperature constant (100 MPa and 1200 K, respectively). This resulted in a lattice parameter of .43765 nm and a

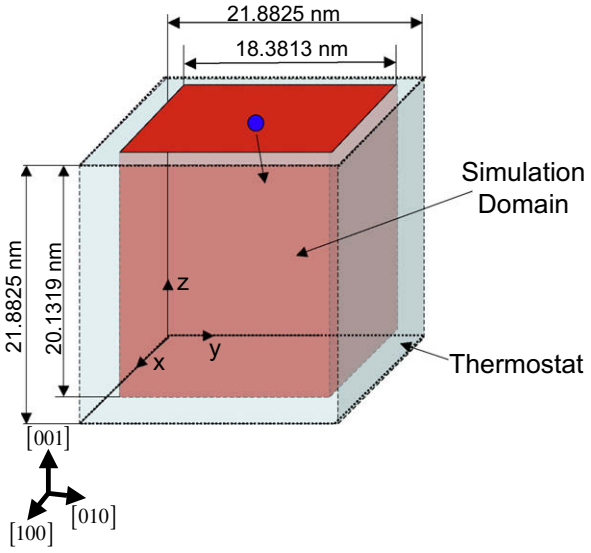

Fig. 2. Schematic of the geometry used for the simulations. The circle represents the PKA initial position.

simulation cell length of about 21.9 nm. For reference, we calculated the 0 K lattice parameter to be approximately .4279 nm with the same potential.

For the PKA we chose a Si atom from the top-center of the simulation cell, based on the description in [22]. As in [22], we imparted the 10 keV PKA kinetic energy in the form of an instantaneous velocity (after thermal equilibration) of 262 nm/ps along the $[4\,11\,\bar{9}5]$ direction (just off of the Z-direction). Following [22], we chose this direction to minimize the likelihood of the PKA channeling early in the cascade formation. A schematic of the system is given in Fig. 2.

2.1. Interatomic interactions

We modeled the interatomic interactions with a hybrid Tersoff/ZBL potential, similar to the hybrid potential described in [18] and [23] with Tersoff potential parameters from [18] (see Table 1). The resulting potential was of the following form,

$$E = \frac{1}{2}\sum_i \sum_{j\neq i} U_{ij}, \tag{1}$$

$$U_{ij} = [1 - f_F(r_{ij})]U_{ij}^{\mathrm{ZBL}} + f_F(r_{ij})U_{ij}^{\mathrm{Tersoff}}, \tag{2}$$

$$f_F(r_{ij}) = \frac{1}{1 + e^{-A_F(r_{ij}-r_C)}}, \tag{3}$$

$$U_{ij}^{\mathrm{ZBL}} = \frac{1}{4\pi\epsilon_0}\frac{Z_i Z_j e^2}{r_{ij}}\phi\left(\frac{r_{ij}}{a}\right), \tag{4}$$

$$a = \frac{0.8854 a_0}{Z_i^{0.23} + Z_j^{0.23}}, \tag{5}$$

$$\phi(x) = 0.1818e^{-3.2x} + 0.5099e^{-0.9423x} + 0.2802e^{-0.4029x} + 0.02817e^{-0.2016x}. \tag{6}$$

The tunable parameter A_F in the Fermi function, f_F, controls the 'sharpness' of the transition from one potential to the other, and r_C controls the radius at which the transition occurs. We chose $A_F = 140\ \mathrm{nm}^{-1}$ and $r_C = .095$ nm based on [18]. As usual, r_{ij} is the distance between the particles' centers of mass, ϵ_0 is the permittivity of a vacuum (.000552635 e/(eV nm)), e is the electron charge, and Z_i and Z_j are the number of protons in each nucleus.

2.2. Simulation phases

Our simulations used the following multiple-phase timestep procedure, based on the phases of cascade formation described in [1,26]. We verified this procedure by checking the maximum system velocity at 100 timestep intervals to ensure that the maximum displacement in a given timestep was less than 1/5 of the nearest neighbor distance.

- Thermal equilibration, part 1. All atoms in the system have their velocity scaled every step to maintain the desired nominal temperature. System allowed to equilibrate for 1000 timesteps with a 1 fs timestep (1 ps total time).
- Thermal equilibration, part 2. Interior region (everything except the 4 cell thermostat skin) thermostat removed. Thermostat skin maintained at desired temperature. System allowed to equilibrate for 1000 timesteps with a 1 fs timestep (1 ps total time).
- Initial collision phase (labeled in later diagrams as I). PKA instantaneous velocity applied (but not maintained). System allowed to evolve for .2 ps (20000 timesteps with a .01 fs timestep).
- Intermediate evolution phase (labeled in later diagrams as II). System allowed to evolve for 1 ps (10000 timesteps with a .1 fs timestep).
- Final evolution phase (labeled in later diagrams as III). System allowed to evolve for 10 ps (10000 timesteps with a 1 fs timestep). Total time from PKA excitation to end of this phase: 11.2 ps.

2.3. Post-processing

Molecular dynamics simulations are based on the evolution of the positions, velocities and forces associated with points representing atomic nuclei. Therefore, it is usually necessary to perform some 'post-processing', calculations or data manipulations after the solution phase of the calculation, to obtain useful information from the simulation. The information we extracted from our simulations included:

- PKA kinetic energy as a function of time.
- PKA displacement as a function of time.
- Point defect configuration visualization.
- Number of point defects as a function of time.
- Number and size of point defect clusters as a function of time.
- Radial distribution function (RDF) for vacancies.
- Spatial distribution of vacancies in simulation cell.

Additionally, due to the chaotic nature of displacement cascades it is necessary to consider not only information from individual simulations, but also this information averaged over a number of runs. In the results, the bulk of the quantitative data presented has been averaged over the number of runs that did not exhibit clear 'wrap-around' of the PKA or cascade. In other words, we neglected the runs where the cascade interacted directly with the thermostat and periodic boundaries. This was a similar approach to that taken in [22]. We chose this approach because the results of these wrap-around runs were unphysical due to the thermostat interaction effects. Further, a simulation domain where such events would not occur would be prohibitively large, as a minimum size cannot be calculated *a priori* for a given PKA kinetic energy. Finally, a reduction in the PKA kinetic energy to ensure the cascades were fully contained would have likely reduced the amount of damage such that measuring cascade differences would have been difficult.

2.3.1. PKA kinetic energy and displacement

In order to get a basic understanding of the behavior of the PKA through the simulated time, it is useful to look at its kinetic energy and displacement. The raw data was obtained by outputting the position and kinetic energy of the PKA (a pre-defined atom) every 100 timesteps. We defined the displacement as the magnitude of the relative position vector with respect to the initial position of the PKA: $|\mathbf{x}(t) - \mathbf{x}(0)|$, where $\mathbf{x}(t)$ indicates position at time t. We tabulated this information at each output step and plotted it in the open-source graphing package gnuplot [27] as a basic X–Y plot.

2.3.2. Point defects and defect cluster identification

Prior to any analysis of point defect data based on an MD simulation, it is necessary to identify these defects as the simulation itself deals only with nuclear positions. The technique we used is based on a Wigner-Seitz (or Voronoi) cell analysis and has been discussed in the literature [28–30]. With this method, we defined point defects based on the number of atoms from the output geometry found in each reference cell (the *occupancy* of the reference cell):

- Occupancy = 0: vacancy site.
- Occupancy > 1: interstitial site.
- Occupancy = 1: normally occupied site. A second check was performed on these sites to find antisite defects and atomic replacement events.

For all of the above cases, we considered the defect site to be located at the center of the corresponding reference cell.

To quantify the distribution of vacancies in the system being studied, we used three approaches. The first method used the identified defect geometry and a given search radius to identify vacancies with neighboring vacancies (i.e., vacancy clusters). For vacancies with neighbors, the search was repeated on the neighbors and so on until no new vacancies were found. Our search radius was chosen to be .22 nm. This value corresponds to the Si–Si cutoff radius for the interatomic potential and is a convenient distance between the first and second neighbor distances. We defined an additional measure, the clustering percentage, as the percentage of the total number of vacancies associated with a cluster. To quantify how isolated an 'isolated' vacancy was during the simulations, we calculated a body-averaged vacancy radial distribution function (RDF) at key output steps. The first step was to create a histogram of the body-averaged distance between vacancies. In order to obtain the RDF from this, we normalized the histogram by the product of the total number of vacancies (n_{vac}) in the system minus one (each vacancy has a total of $n_{vac} - 1$ neighbors) and the number of atoms at each separation distance in a perfect crystal. The resulting data from these calculations were plotted in a similar manner to the PKA data.

3. Results and discussion

Our simulations were performed with the Sandia National Laboratories Large-scale Atomic/Molecular Massively Parallel Simulator code (LAMMPS) [31]. After the initial configurations were generated, a total of 20 runs at 1200 K were performed and 10 each at 0 K, 10 K, 100 K, 500 K and 2000 K. At each temperature we used the same PKA initial conditions, described earlier. Each run was given different thermostat initial conditions such that the initial positions and velocities varied while keeping the target temperature and initial conditions of the systems statistically equivalent. We did this in LAMMPS by providing different random number generator seeds to the velocity scaling thermostat function in the input files.

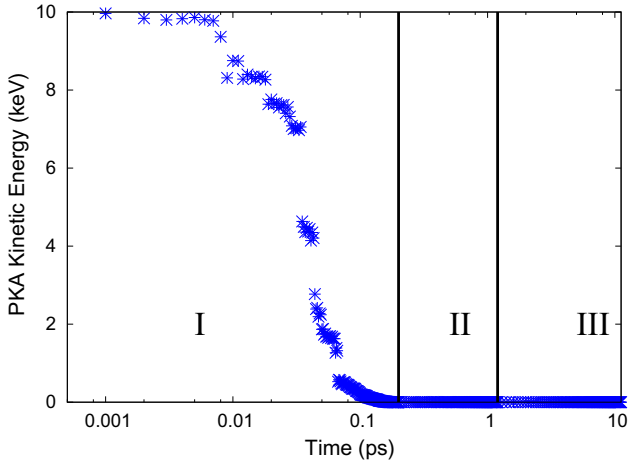

Fig. 3. Example of the PKA kinetic energy through the simulation time, from a simulation at 1200 K. In all cases where there was no interaction with the boundaries, over 99.99% of the kinetic energy applied to the PKA was dissipated by the end of phase I.

3.1. PKA displacement

Once the simulations were completed and post-processed, we examined the evolution of the PKA. At every temperature, we found the decay of the PKA kinetic energy to be nearly identical. Thus, only a single example is shown in Fig. 3 to illustrate the typical response. By the end of phase I, the PKA had lost over 99.99% of its initial kinetic energy and by the end of phase II it had reached the thermal background energy. However, there are other aspects of the PKA evolution that merit discussion, such as the number of wrap-around events and PKA displacement.

Fig. 4 shows the percentage of the runs at each temperature that demonstrated PKA 'wrap-around'. Fig. 5 presents the average and spread of final PKA displacements for each temperature. At 0 K all of the PKA displacements were identical, approximately 10 nm, and exhibited no wrap-around. This is not surprising given that the relative positions of the atoms in each run would be identical because the random number generator only impacts the initial velocities, all of which would be identically 0 at 0 K. However, as the temperature (and therefore relative atomic displacements) increases to above 0 K, we see the development of a spread of final PKA displacements by 10 K. Fig. 5 shows that the

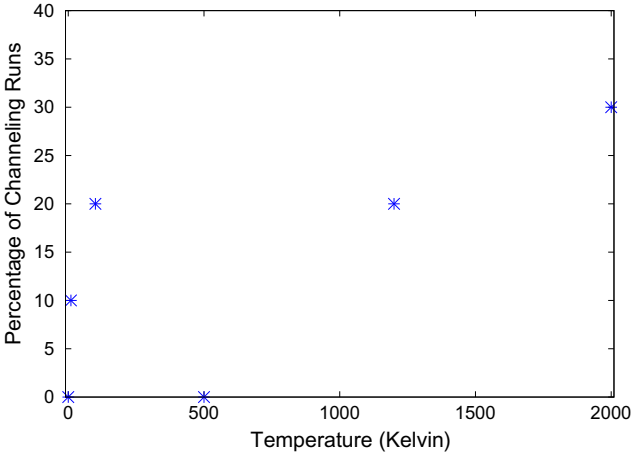

Fig. 4. The percentage of runs that exhibited wrap-around of the PKA (i.e. possible PKA channeling) at each temperature. Percentage used as the 1200 K case consisted of 20 runs while the others consisted of 10.

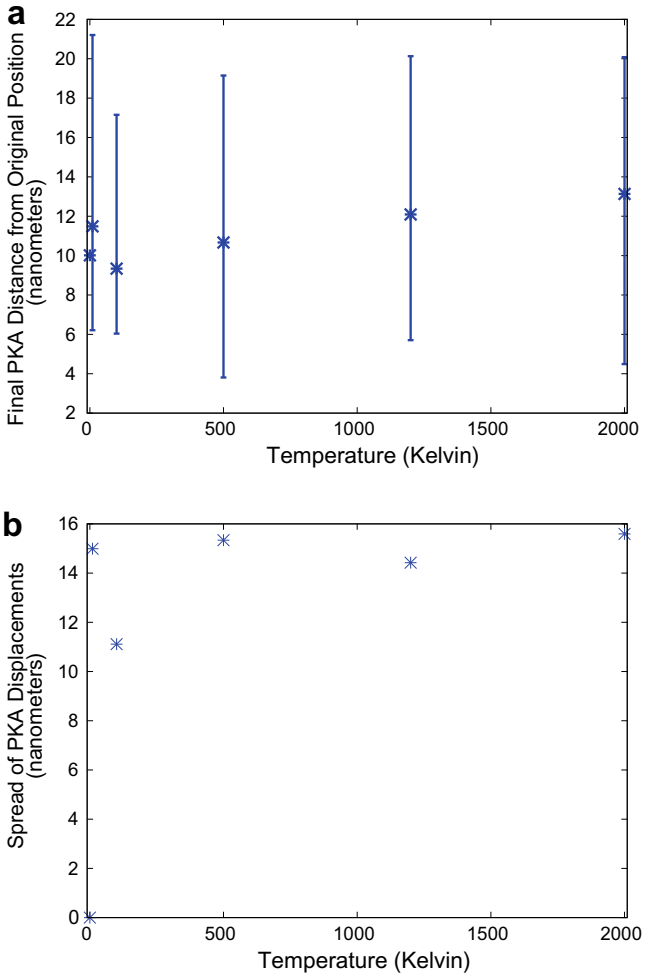

Fig. 5. Plot of the final PKA displacement, averaged for all non-wrap-around runs at each temperature. The error-bars show the spread of the data at each temperature. Note that the spreads for the non-zero temperatures are nearly the same though the average changes.

spreads remain similar for nearly all of the non-zero temperatures simulated. If the 100 K spread is taken as an outlier, we can conclude that the PKA displacement spread for non-zero temperatures has no dependence on temperature.

3.2. Point defect counts

Next we examined the number of point defects through the simulated time and temperatures. We obtained the following plots by averaging over the data from all of the non-wrap-around runs at each temperature.

Fig. 6 illustrates the run-averaged total number of vacancies at each temperature through the simulation time. From the figure, it is clear that there is only a small variation (roughly 20 vacancies) in the 0 K through 1200 K cases. The 2000 K case is different from the others, though it only varies by a maximum of 47 vacancies (~27%) at the peak and 16 (~10%) at the last step. However, unlike the other cases, the number of vacancies is decreasing throughout phase III. By comparing each individual run at each temperature, we found that the total defect variations in Fig. 6 were within the variation seen between runs at the same temperature. The exception was the 0 K case, where all runs yielded the same defect evolution. Despite this, there is a clear difference in the 2000 K case that suggests different defect evolution behavior. Similarly, if one

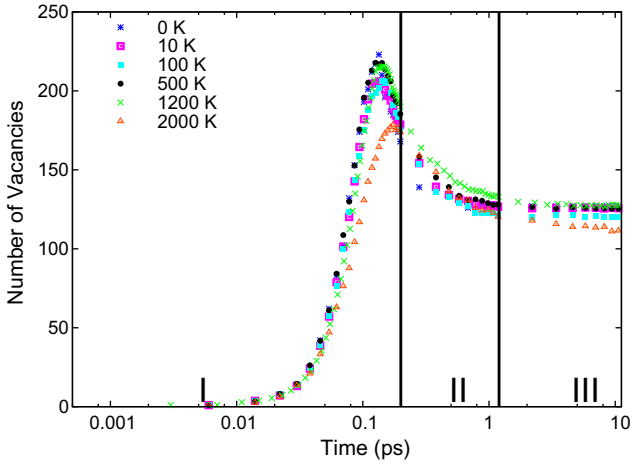

Fig. 6. Plot of the run-averaged total vacancy counts for each temperature. Note that the only significant difference is in the 2000 K case.

examines Fig. 7, there is no clear trend and the variations are within that seen in individual runs at a given temperature. The 2000 K case exhibited different behavior in the individual vacancy counts, just as it did in the total counts. Further, it is clear that the decrease in the total number of vacancies in phase III is due to a decrease in

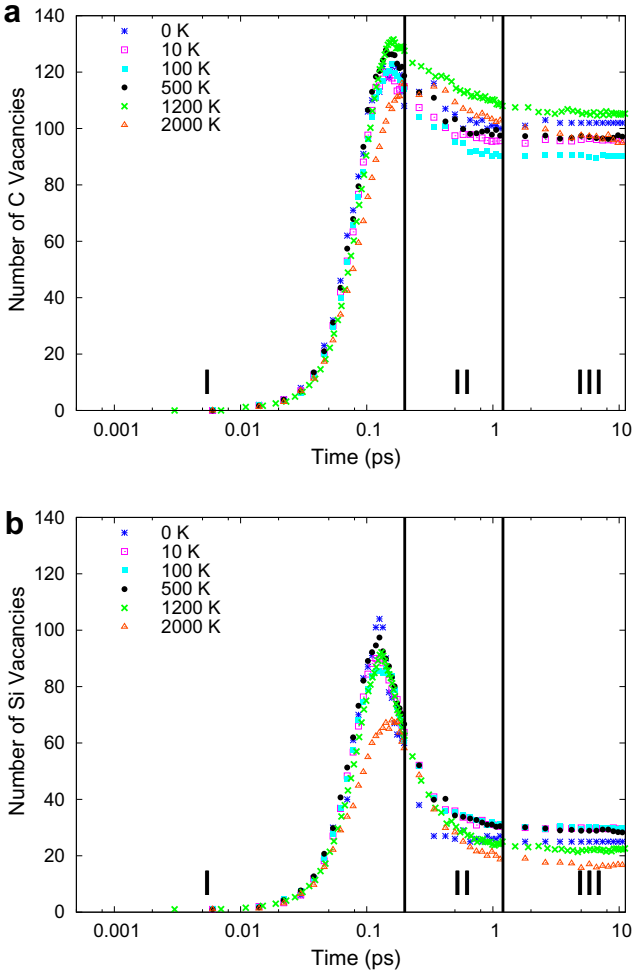

Fig. 7. Plot of the run-averaged vacancy counts for each temperature and atom type. There is little indication of temperature dependence by this measure.

the number of C vacancies. We attribute this to C interstitial–vacancy recombination, as the thermal background energy at 2000 K is on the order of the migration barrier for C interstitials (roughly .75 eV [32]). Despite this difference at the highest temperature, we concluded that there is no clear temperature dependence in the total number of vacancies nor the number of each type generated. The differences in the 2000 K case indicated to us the existence of a high-temperature cascade regime, where thermal effects decrease the effective damage due to the cascade. However, further study of this high-temperature regime is left for future work.

The number of vacancies only tells part of the story. Thus it is useful to look at other defect types such as antisite defects and atomic replacements, shown in Figs. 8 and 9, respectively. Unlike the vacancy counts, these plots do show trends that indicate a temperature dependence. The number of C_{Si} antisites generated in the intermediate and final evolution phases (II and III) clearly increases with temperature, and only in the 0 K case does the number clearly decrease from the value at the end of initial collision phase (I). Further, while the 0 K through 1200 K cases seem to have leveled out, the 2000 K case appears to increase throughout phase III. Meanwhile, we find less indication of temperature dependence on the formation of Si_C defects. In particular, the maximum number formed is nearly constant through all temperatures, though the final number increases with temperature (except in the 2000 K case). In all cases, there is some amount of relaxation that occurs in phases II and III, though this effect is slightly reduced at higher

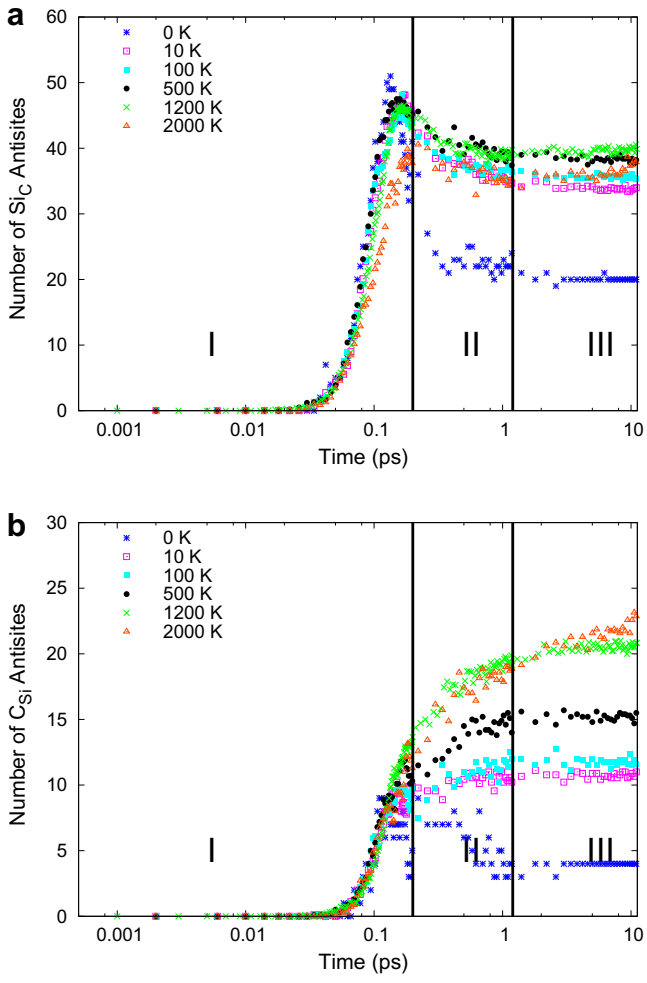

Fig. 8. Plot of the run-averaged antisite defect counts for each temperature and defect type.

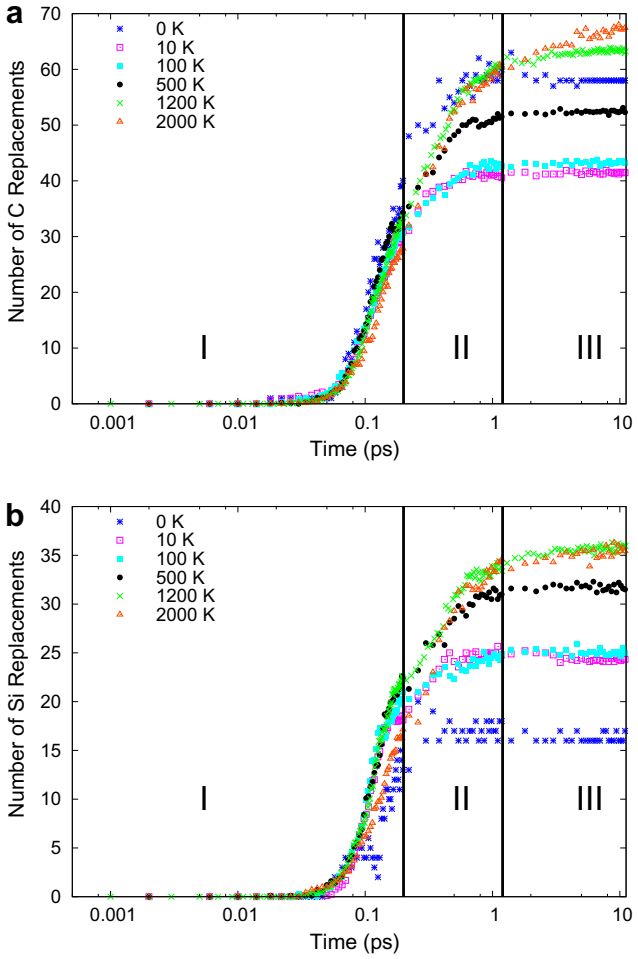

Fig. 9. Plot of the run-averaged atomic replacement events for each temperature and defect type.

temperatures. For nearly all the temperatures (0 K C_{Si} defects are the exception), the relative stability of the antisites formed may be explained by the fact that forming an antisite defect from an existing interstitial–vacancy pair is energetically favorable [33]. However, this does not explain the decrease in the number of Si_C defects in phase II. The decrease in Si_C defects is possibly due to thermal vibrations 'kicking' the Si atom out of the C site, allowing a nearby C atom to form a replacement. We find similar trends in Fig. 9, where the number of C and Si replacements after phase I increases with temperature; though more C replacements were seen at 0 K than at 10 K and 100 K. For all temperatures, more C replacements were found than C_{Si} antisites, while the number of Si replacements and Si_C antisites differed by roughly 33%. Finally, we concluded that the increase in the number of C replacements in phase III with increasing temperature is further evidence of the role of thermal vibrations in C vacancy–interstial annihilation during cascade evolution. Further study of this effect, along with the role of antisite formation and antisite-replacement swapping in cascade relaxation is needed.

3.3. Vacancy clusters and distributions

The final aspect of the simulations that we examined is the vacancy clustering data as a function of time and temperature. The average vacancy cluster number and size are given in Figs. 10 and 11, respectively. The clustering percentage data is given in Fig. 12.

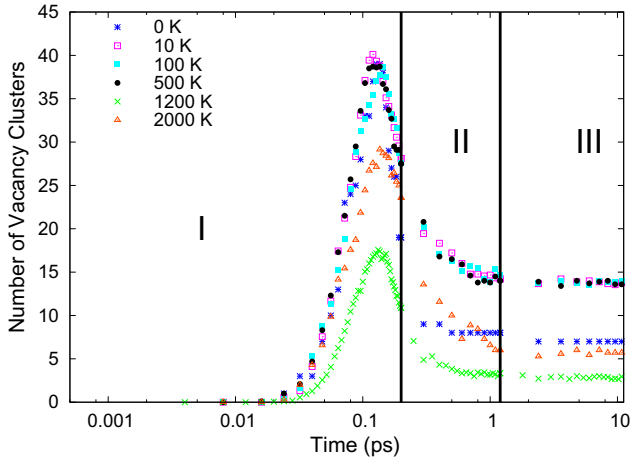

Fig. 10. Plot of the run-averaged number of vacancy clusters for each temperature.

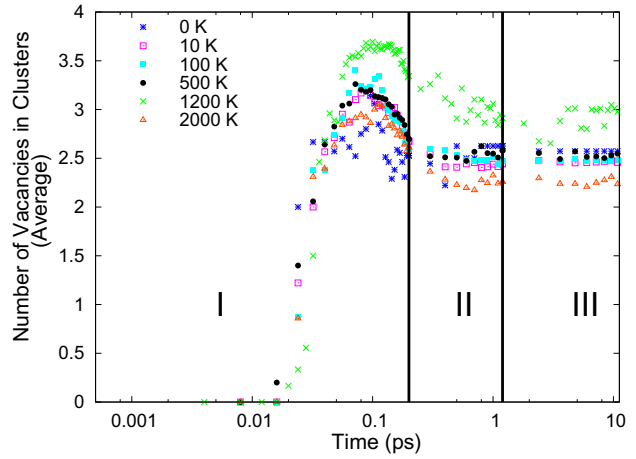

Fig. 11. Plot of the average vacancy cluster size (number of vacancies per cluster) for each temperature.

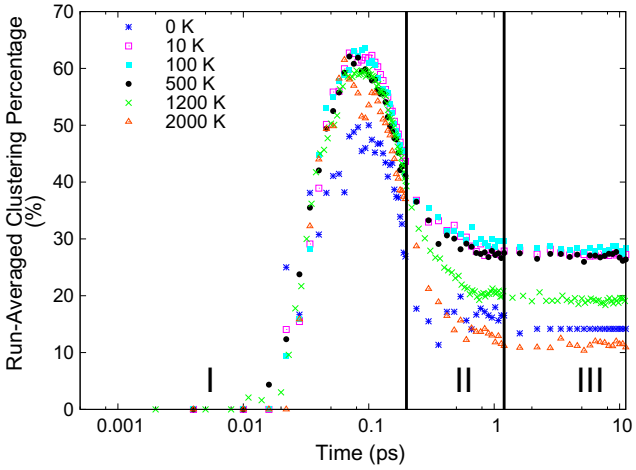

Fig. 12. Plot of the average percentage of vacancies found in clusters at each temperature.

From an examination of Fig. 10, we see that the final number of clusters increases as the temperature increases from 0 K to 500 K, after which the number drops. Thus, at the highest temperatures there are only a few vacancy clusters (an average of about 3–5 clusters). Further, Fig. 11 shows that the average cluster size is between 2 and 4 vacancies for all temperatures. This indicates that at the higher temperatures, only a few stable clusters form and those are clusters of only a few vacancies, thus few vacancies are associated with clusters. A possible reason for this is that the thermal energy allows for greater defect and atomic mobility, thus there is more energy available to 'breakup' unfavorable defect configurations. This possibility is further evidenced by the fact that the number and average size of the vacancy clusters is nearly constant after phase II, when the cascade has dissipated most of its energy and the system approaches a stable configuration through thermally driven defect migration and annihilation. These findings agree well with those of [23].

The results from the previous paragraph led us to the question of what percentage of the vacancies in the system are actually in clusters as opposed to isolated or in bound interstitial–vacancy pairs. Fig. 12 answers this question. There are two points of note in this figure. Firstly, the peak percentage is roughly the same for all temperatures and occurs at very nearly the same time. This time corresponds to the maximum number of defects generated, i.e., the peak of the cascade formation from Fig. 6. There is a similar trend to that seen in Fig. 10: the final percentage of clustered vacancies increases from about 12% at 0 K to about 30% at 100 K, when it steadily decreases until the lowest value of roughly 10% is reached at 2000 K. These results indicate the possibility of a moderate temperature at which a maximum amount of clustering occurs in the simulated timescale. These findings reinforce our earlier finding that the bulk of the vacancies in the final defect configuration are isolated from one another, and that this is the case regardless of the temperature. In fact, at the lower temperature ranges upwards of 70% of vacancies are isolated, while at the highest temperatures this is magnified to 80–90% isolated vacancies.

In order to elucidate the thermal effects on the final spatial distribution of vacancies, we calculated a vacancy RDF for each run using a bin width of .1 nm and averaged it over the non-wrap-around runs at each temperature. This data is provided in Figs. 13 and 14. For the temperature range of 10–1200 K there is little significant variation in the RDF except at distances of less than .2 nm and greater than 4 nm. At the end of the simulation (see Fig. 13), the 2000 K case indicates a wider distribution of vacancy separations than other temperatures, despite appearing similar or lower than the other temperatures in the figures shown. This is because of the normalization of the figure, which was chosen such that the integral of the RDF must be the same for all temperatures. Therefore, since the 2000 K RDF is generally smaller in all of the plotted regions, there must be more vacancies at separations greater than about 7 nm. For comparison, the furthest apart vacancies could be in this system is roughly 31.6 nm. Finally, Fig. 14 shows the RDF for the 500 K and 2000 K cases at the end of phases I and III. These plots indicate that there is a reduction in the number of close-paired vacancies (i.e. those separated by less than about .4 nm), while the number of longer range pairs increases for nearly the entire range plotted. Similar trends are seen at the other temperatures. The reduction in the number of close-paired vacancies is most dramatic (almost 50%) at 2000 K.

We believe it is unlikely that thermal diffusion alone accounts for the differences seen in the figures, as even at 2000 K few atoms would have the kinetic energy to overcome the high potential energy barriers for bulk vacancy diffusion (roughly 4.1 eV and 2.3 eV for C and Si vacancies, respectively [32]) during the timescale of the simulations. Further, the final value for the total number of vacancies in the 2000 K case was smaller than all of the other temperatures. Thus, we conclude that recombination of interstitial/vacancy pairs during cascade formation plays a greater role than bulk vacancy diffusion, as interstitials are known to be more mobile than vacancies in SiC [32]. Specifically, at 2000 K it is more likely

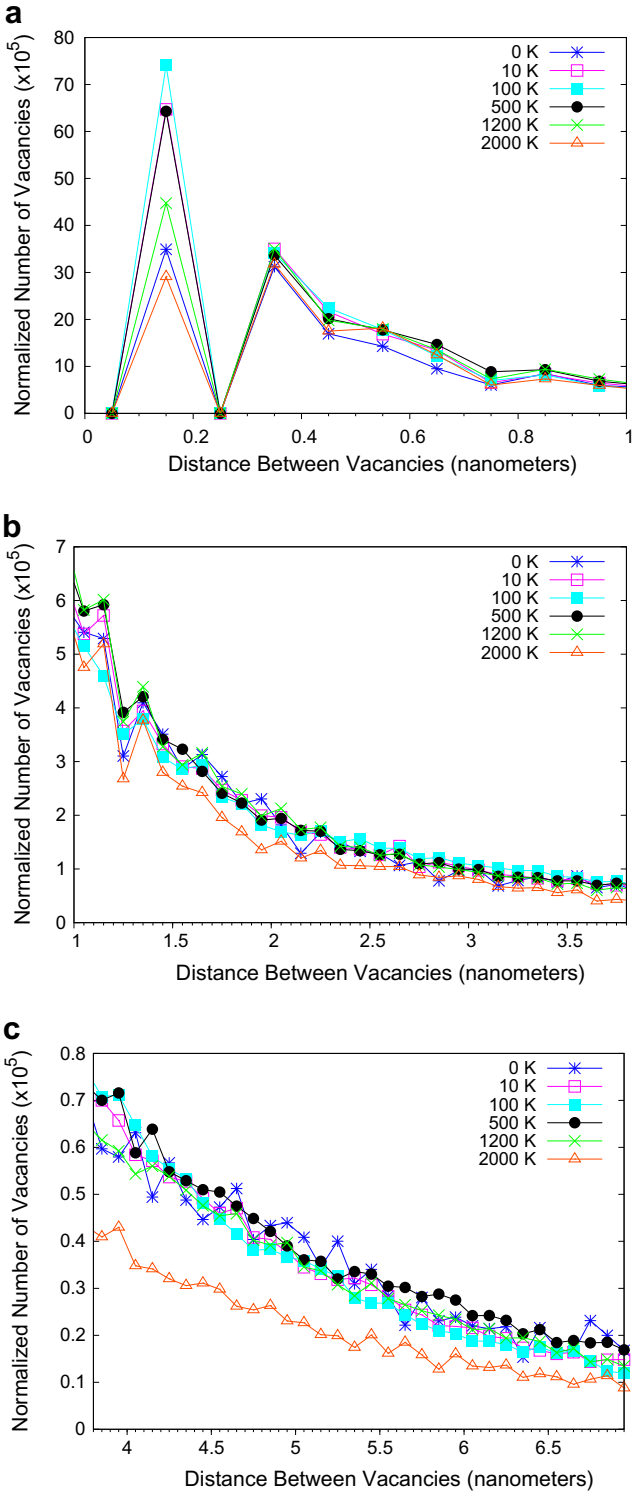

Fig. 13. Plot of the averaged vacancy radial distribution function for each temperature at the end of the simulation. (a) shows the detail of the RDF for separations less than 1 nm. The normalization factor is $n_{vac} - 1$ times the number of atoms in each bin in a perfect crystal. The width of the bins for the RDF is.1 nm.

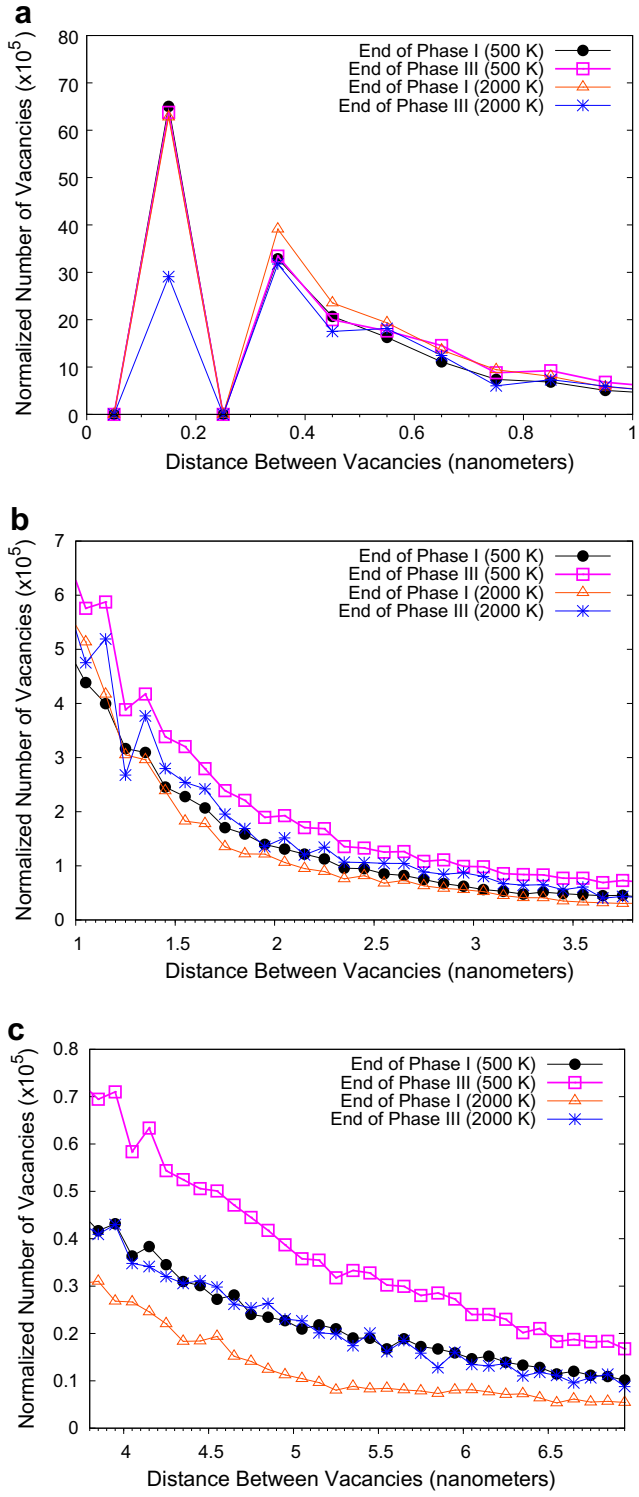

Fig. 14. Plot of the run-averaged vacancy radial distribution function for the 500 K and 2000 K cases at the end of the initial collision (I) and the final evolution (III) phases.

that an atom would have a kinetic energy on the order of the interstitial migration barriers (roughly .75 eV and 1.5 eV for C and Si interstitial sites, respectively, [32]) than at lower temperatures. This would also explain the decrease in the total number of vacancies and interstitials during phase III for only the 2000 K case, as shown in Fig. 6.

Our final point of comparison was the final spatial distributions of vacancies. These results are illustrated in Fig. 15. There is little clear indication of temperature dependence in the final configuration, and the distributions are largely similar. There is some indication of a trend towards more diffuse damage in the *Z*-direction as temperature increases, though the difference is only on the order of 1% between the low and high temperature cases.

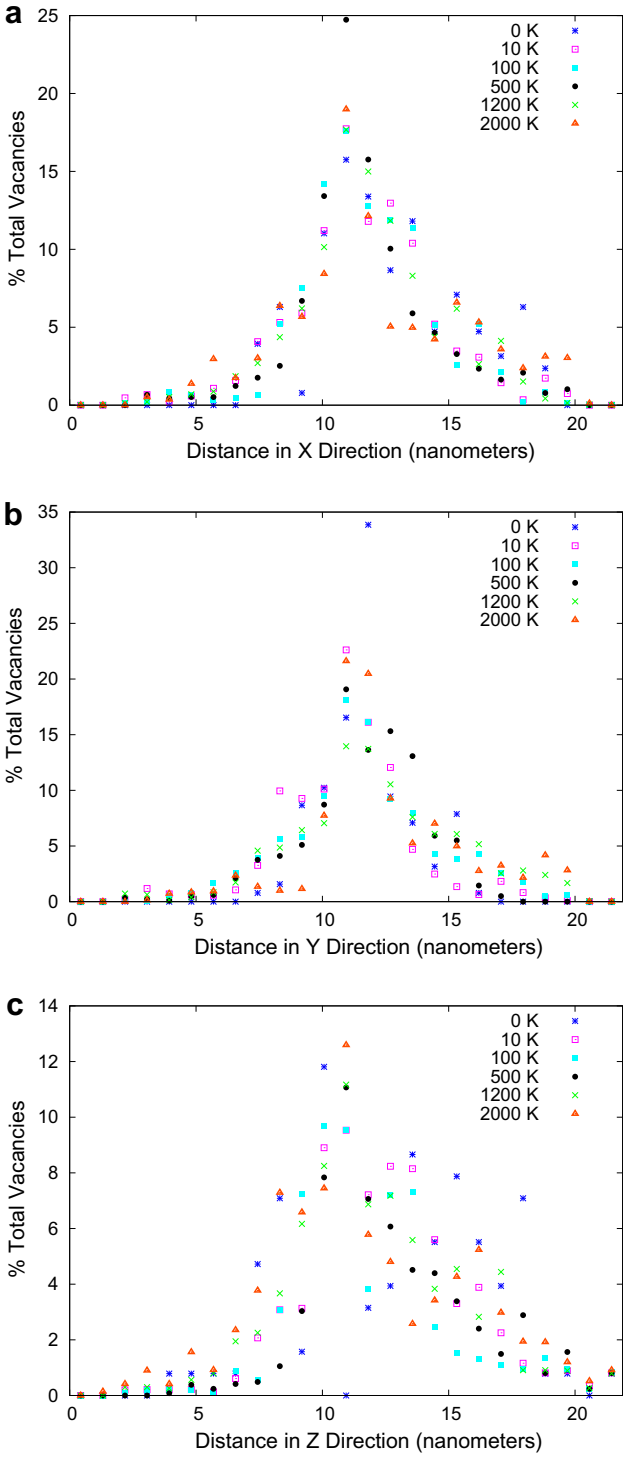

Fig. 15. Plots of the final vacancy spatial distribution for each temperature and direction.

4. Conclusions

The temperature study performed yielded several interesting points. The first was that we found the PKA behavior to be largely independent of temperature. At 0 K there was no spread in the response of the PKA and the spread at higher temperatures had little variation. Our study of point defect generation and evolution behavior indicated the possible role of enhanced C interstitial–vacancy recombination in cascade relaxation at 2000 K, a phenomenon that was not readily apparent at lower temperatures. We speculate that this could lead to considerable cascade annealing at high temperatures, over timescales unreachable by MD simulations. Beyond this, we found little indication of temperature dependence in the number of vacancies and Si_C antisites generated. On the other hand, C and Si replacements and C_{Si} antisite formation did show temperature dependence. We observed that the number of C and Si replacements increased non-linearly with temperature. The number of C_{Si} antisites was significantly higher at higher temperatures, likely due to enhanced C interstitial mobility. Our analysis of vacancy clusters indicated that regardless of temperature, the number of vacancies found in clusters was relatively small (10–30% of the total number of vacancies). Additionally, we found little evidence of temperature dependence in the final relative distribution of vacancies at small distances (less than 1 nm). Despite this, we found indications of a wider distribution of vacancies at 2000 K. We concluded that this was further evidence of the existence of a high-temperature regime where atomic and defect mobility effectively decreases the amount of concentrated damage during cascade formation. Based on our results, we expect little vacancy cluster growth on longer timescales due to vacancy migration. However, additional PKA excitation events and subsequent cascade overlap would be expected to increase the number of initially clustered vacancies. We also conclude that more work is needed to provide further evidence for this as well as the mechanisms involved in high-temperature relaxation, such as antisite defect creation from mixed vacancy–interstial pairs. Finally, we expect that a more complete study including PKA direction variations and much larger simulation cells will soon be possible thanks to ever increasing supercomputing and distributed post-processing capabilities.

Acknowledgements

The support of Wing Kam Liu and David Farrell by the National Science Foundation (NSF), the NSF-IGERT and NSF-Naval Civilian Services Grants and Northwestern University, and the support of Noam Bernstein by the Office of Naval Research, the Naval Research Laboratory, are gratefully acknowledged. The authors would also like to acknowledge the Department of Defense High Performance Computing Modernization Program and the Army Research Laboratory Major Shared Resource Center for the HPC systems used in the course of this work.

References

[1] A.M. Stoneham, C.A. English, W.J. Phythian, Radiat. Eff. Defect. Solid 144 (1998).
[2] M.W. Thompson, Defects and Radiation Damage in Metals. Cambridge Monographs on Physics, first Ed., Cambridge University, 1969.
[3] P. Sigmund, Rev. Roum. Phys. 7 (1972).
[4] S.J. Zinkle, C. Kinoshita, J. Nucl. Mater. 251 (1997).
[5] Higher Temperature Reactors Materials Workshop, in: Proceedings of DOE Workshop, La Jolla CA, 18–21 March 2002.
[6] A. Hasegawa, A. Kohyama, R.H. Jones, L.L. Snead, B. Riccardi, P. Fenici, J. Nucl. Mater. 283 (2000).
[7] B. Riccardi, L. Giancarli, A. Hasegawa, A. Katoh, A. Kohyama, R.H. Jones, L.L. Snead, J. Nucll Materl 329–333 (2004).
[8] Scientific Issues & Technological Challenges in the Development of Materials, in: Proceedings of the 2004 Fredric Joliot & Otto Hahn Summer School, Cadarache, France, 25 August–3 September, 2004.
[9] R. Blackstone, E.H. Voice, J. Nucl. Mater. 39 (1971).
[10] J.E. Palentine, J. Nucl. Mater. 61 (1976) 243.
[11] A.I. Ryazanov, A.V. Klaptsov, A. Kohyama, H. Kishimoto, J. Nucl. Mater. 307–311 (2002) 1107.
[12] R.J. Price, J. Nucl. Mater. 48 (1973) 47.
[13] Y. Katoh, N. Hashimoto, S. Kondo, L.L. Snead, A. Kohyama, J. Nucl. Mater. 351 (2006) 228.
[14] Workshop on Advanced Computational Materials Science: Application to Fusion and Generation IV Fission Reactors, in: Proceedings of DOE Workshop, Washington DC, 31 March–2 April, 2004.

[15] B. Raj et al., Challenges in Materials Science Research for Sustainable Nuclear Energy, MRS Bulletin, 33, Special Issue on Harnessing Materials for Energy, April, pp. 327–337, 2008.
[16] H. Huang, N. Ghoniem, J. Nucl. Mater. 212–215 (1994) 148.
[17] J. Wong et al., J. Nucl. Mater. 212–215 (1994) 143.
[18] R. Devanathan, T. Diaz de la Rubia, W.J. Weber, J. Nucl. Mater. 253 (1998) 47.
[19] H. Hensel, H.M. Urbassek, Nucl. Instrum. and Meth. B 142 (1998).
[20] J. Tersoff, Phys. Rev. B 39 (1989).
[21] J.F. Ziegler, J.P. Biersack, U. Littmark, The Stopping and Ranges of Ions in Solids, vol. 1, Pergamon, 1985.
[22] R. Devanathan, W.J. Weber, T. Diaz de la Rubia, Nucl. Instrum. and Meth. B 141 (1998) 118.
[23] J.M. Perlado, L. Malerba, A. Sanchez-Rubio, T. Diaz de la Rubia, J. Nucl. Mater. 276 (1–3) (2000) 235.
[24] F. Najmabadi et al., Fus. Eng. Des. 80 (1) (2006).
[25] WebElements online periodic table and atomic information. <http://www.webelements.com/>.
[26] E. Friedland, Crit. Rev. Solid State Mater. Sci. 26 (2) (2001).
[27] gnuplot: open source graphing application website. <http://www.gnuplot.info/>.
[28] J.B. Gibson, A.N. Goland, M. Milgram, G.H. Vineyard, Phys. Rev. 120 (4) (1960) 1229.
[29] K. Nordlund et al., Phys. Rev. B 57 (13) (1998) 7556.
[30] S.M. Foiles, Nucl. Instrum. and Meth. B 255 (2007) 101.
[31] Large-scale Atomic/Molecular Massively Parallel Simulator (LAMMPS) website. <http://lammps.sandia.gov/>.
[32] F. Gao, W.J. Weber, Phys. Rev. B 69 (2004) 224108.
[33] F. Gao, E.J. Bylaska, W.J. Weber, L.R. Corrales, Phys. Rev. B 64 (2001) 245208.